Domain-wall-induced electromagnons in multiferroics

S. Omid Sayedaghaee,[1] Sergey Prosandeev,[1] Sergei Prokhorenko,[1] Yousra Nahas,[1] Charles Paillard,[2] Bin Xu,[3] and L. Bellaiche[1]

[1]*Physics Department and Institute for Nanoscience and Engineering, University of Arkansas, Fayetteville, Arkansas 72701, USA*
[2]*Laboratoire Structures, Propriétés et Modélisation des Solides, CentraleSupélec, CNRS UMR 8580, Université Paris-Saclay, 91190 Gif-sur-Yvette, France*
[3]*Institute of Theoretical and Applied Physics and School of Physical Science and Technology, Soochow University, Suzhou, Jiangsu 215006, China*

(Received 8 November 2021; revised 28 February 2022; accepted 1 March 2022; published 21 March 2022)

Using an atomistic approach, we predict the emergence of hybrid quasiparticles, namely, *domain-wall-induced* electromagnons, that arise from dynamical couplings between magnons and optical phonons in systems possessing ferroelectric domain walls. These quasiparticles induce THz resonances in magnetoelectric responses and preferentially localize either near the domain walls or near the middle of domains. Such behavior is explained through dispersion analysis that allows us to track the emergent multidomain excitations back to single-domain magnetoelectric (ME) modes. The latter, scattered by a periodic array of domain walls, are shown to endow the domain-wall-induced electromagnons with a mixed localized mode and standing- or propagating-wave characters. Such features can be exploited to reach strikingly large ME conversion and design more reliable and ultrafast ME devices with less energy consumption and using, e.g., local probes.

DOI: 10.1103/PhysRevMaterials.6.034403

I. INTRODUCTION

Recent observations of magnetoelectric (ME) responses in multiferroics, which characterize cross couplings of electric and magnetic properties, have reawakened the interest of scientists and engineers in this territory of research, particularly in the last two decades [1–5]. Such cross couplings open opportunities to, e.g., control electrical polarization by magnetic field or magnetization by electric field. Switching of polarization by magnetic field can be employed technologically in the design of memory devices and magnetic field sensors whereas switching of magnetization by electric field is useful in designing low-energy consumption storage devices in which data is written electrically and read magnetically [5–11]. The existence of excitations other than phonons, such as magnons, in these systems provides more functionalities such as controlling the spin waves by electric field or by optical phonons [6,12,13]. The dynamical ME couplings of magnons and phonons, known as electromagnons, have also attracted considerable attention due to their role in magnetocapacitance and magnetodielectric effects [14–17]. Starting in 2006, experimental reports such as exciting spin waves by light in $TbMnO_3$ [18] and activating magnetic excitations by applying electric fields in YMn_2O_5 and $TbMn_2O_5$ [19] kicked off investigations on the origin and mechanism of electromagnons. In particular, it was also experimentally shown that adjusting Terahertz pulses with electromagnons of 0.7 and 1.8 THz in $TbMnO_3$ can affect its magnetic structure [20]. In 2008, electromagnons were proposed to be observed for the first time in single crystals [21,22] and thin films [23] of bismuth ferrite $BiFeO_3$ (BFO). Atomistic methods also predicted electromagnons in antiferromagnetic ferroelectrics [24]. A dynamical coupling of magnons with acoustic phonons and optical phonons, coined as electroacoustic magnons, was also suggested in 2019 [25,26]. Electromagnons can have other benefits. For instance, switching the orientation of domains by applying electric fields on multiferroics is typically of the order of milliseconds [20,27], although the speed of ferromagnetic or ferroelectric domain reorientation (which is a key in the design of data storage devices) is typically of the order of nanoseconds [20]. To improve the operation speed of devices, one can apply high-frequency magnetic fields or optical pulses which increase the functionality speed to the order of femtoseconds to picoseconds [28–30] or *coherently excite electromagnons* [31]. Based on the latter possibility, and also to advance fundamental knowledge, it is timely to address a presently unknown issue regarding electromagnons, namely, if they can also be preferentially localized within the walls of ferroelectric domains (or near the middle of the domains) rather than only equally vibrate in the entire system. If such preferential localizations exist, novel effects can emerge. Examples include new resonances in the ME responses and/or a local control of the dynamical conversion between electric and magnetic properties. To resolve the aforementioned issues, we performed molecular dynamics (MD) simulations within the GHz-THz regime of applied magnetic fields in BFO materials possessing ferroelectric domain walls. Fourier analyses of temporal evolution of electric dipoles and magnetic moments along with the calculations of quadratic ME response of BFO reveal that the existence of domain walls does result in the emergence of *domain-wall-induced electromagnons*, which in turn induce large enhancement of ME response around their resonances. These quasiparticles were further found to either be preferentially localized near the domain walls or near

the center of the domains (depending on their frequency and direction of propagation of their optical phonon and magnon), as a result of scattering by the periodic array made by the domain walls. Such discoveries have the potential to pave the way for designing original devices. For instance, although the capabilities of magnons as the carriers of information in the field of magnonics is quite promising [32], one of the main challenges is to find a way to control the two-dimensional propagation of the magnons in an energy-efficient fashion, especially in small length scales. A previously proposed approach, which was also realized in experiments recently [33], is to guide the spin-waves in a reconfigurable domain wall as magnonic waveguides. Here, the present paper revealing the existence of domain-wall-induced electromagnons strongly suggests that magnonic circuitry can be utilized by activating, *via electric fields,* the magnons associated with such preferentially localized electromagnons. This should allow us to design configurable electronic circuits with much less energy consumption.

The paper is organized as follows. Section II details the method used here, while results are presented and discussed in Sec. III. Finally, Sec. IV provides a summary of this paper.

II. METHODS

An effective Hamiltonian framework developed for bismuth ferrite and detailed in Ref. [34] is employed to perform MD simulations for the investigation of the temporal evolution of polarization and magnetization as well as the quadratic ME response of BFO (which is one of the few materials with ME functionalities at room temperature, making it a prime candidate for designing novel devices [10,35–37]) under the application of magnetic fields with various frequencies from 10 to 1300 GHz. Note that the applied time-dependent magnetic field can generate an inhomogeneous electric field which we neglected here to merely focus on the ME response rather than the polarization caused by the dielectric response of BFO. In addition, modeling such an electric field was not feasible in the simulations because of using periodic boundary conditions in all three Cartesian directions. Note also that our MD simulations are performed at the temperature of 10 K to reduce numerical noises. However, we numerically found that conducting them at room temperature leads to similar results albeit with lower numerical resolutions for the ME coefficients [25].

This presently used effective Hamiltonian scheme encompasses three main energy contributions given by Eq. (1) [13,34,38]:

$$E^{\text{tot}} = E^{\text{FE}}(\{\boldsymbol{u}\},\{\eta_l\}) + E^{\text{AFD}}(\{\boldsymbol{u}\},\{\eta_l\},\{\boldsymbol{\omega}\}) + E^{\text{MAG}}(\{\boldsymbol{m}\},\{\boldsymbol{u}\},\{\eta_l\},\{\boldsymbol{\omega}\}). \quad (1)$$

In Eq. (1), local modes $\{\boldsymbol{u}\}$ are directly related to local electric dipoles. Strain tensor $\{\eta_l\}$ includes both homogeneous $\{\eta_H\}$ and inhomogeneous $\{\eta_I\}$ strains. The tiltings of oxygen octahedra (also known as antiferrodistortive or AFD motions) are denoted by $\{\boldsymbol{\omega}\}$ and the magnetic moments associated with iron ions are denoted by $\{\boldsymbol{m}\}$. Also, in Eq. (1), the first term includes the energy of local modes and elastic deformations that can be written as [39,40]

$$E^{\text{FE}} = E^{\text{self}}(\{\boldsymbol{u}\}) + E^{\text{dpl}}(\{\boldsymbol{u}\}) + E^{\text{dpl}}(\{\boldsymbol{u}\}) + E^{\text{short}}(\{\boldsymbol{u}\}) + E^{\text{elas}}(\{\eta_l\}) + E^{\text{int}}(\{\boldsymbol{u}\},\{\eta_l\}), \quad (2)$$

in which E^{self} is the self-energy of local-modes, E^{dpl} denotes the long-range dipole-dipole interaction, E^{short} is the short-range interaction of soft modes, E^{elas} denotes the contribution of elastic energy, and E^{int} is the interaction of local modes and strain. An extensive overview and explanation on the energy terms of Eq. (2) is provided in Ref. [40].

The second term of Eq. (1), whose energy is only related to AFD motions and their couplings with local modes and strains, is given by

$$E^{\text{AFD}} = \sum_i \left[\kappa_A\omega_i^2 + \alpha_A\omega_i^4 + \gamma_A\left(\omega_{ix}^2\omega_{iy}^2 + \omega_{iy}^2\omega_{iz}^2 + \omega_{ix}^2\omega_{iz}^2\right)\right] + \sum_{ij}\sum_{\alpha\beta} D_{ij\alpha\beta}\omega_{i\alpha}\omega_{j\beta} + \sum_i\sum_{\alpha\beta} C_{l\alpha\beta}\eta_l(i)\omega_{i\alpha}\omega_{i\beta} + \sum_{ij}\sum_{\alpha\beta} K_{ij,\alpha\beta}u_{j,\alpha}\omega_{i,\alpha}\omega_{j,\beta} + \sum_i\sum_{\alpha\beta\gamma\delta} E_{\alpha\beta\gamma\delta}\omega_{i\alpha}\omega_{i\beta}u_{i\gamma}u_{i\delta}, \quad (3)$$

where indices i and j numerate the lattice sites and α, γ, ν, and δ are the Cartesian components. In Eq. (3), the first term shows the contribution of self-energy of the tilting of the oxygen octahedra while the second term shows the contribution of the short-range interactions of AFD motions. The third term shows the coupling of the AFD motions with strain. The fourth and fifth terms show the contributions of trilinear and biquadratic energies coupling the local modes and AFD distortions. More details about AFD energy contributions can be found in Ref. [41]. The third term of Eq. (1) shows the magnetic moments and the coupling of local modes, strain, and AFD motions with magnetic moments as given in the following:

$$E^{\text{MAG}} = \sum_{ij\alpha\gamma} Q_{ij\alpha\gamma}m_{i\alpha}m_{j\gamma} + \sum_{ij\alpha\gamma} S_{ij\alpha\gamma}m_{i\alpha}m_{j\gamma} + \sum_{ij,\alpha\gamma\nu\delta} E_{ij,\alpha\gamma\nu\delta}m_{i\alpha}m_{j\gamma}u_{i\nu}u_{i\delta} + \sum_{ij,\alpha\gamma\nu\delta} F_{ij,\alpha\gamma\nu\delta}m_{i\alpha}m_{j\gamma}\omega_{i\nu}\omega_{i\delta} + \sum_{ijl,\alpha\gamma} G_{ijl,\alpha\gamma}\eta_l(i)m_{i\alpha}m_{j\gamma} + \sum_{ij} L_{ij}(\boldsymbol{\omega}_i - \boldsymbol{\omega}_j)\cdot(\boldsymbol{m}_i \times \boldsymbol{m}_j). \quad (4)$$

In Eq. (4), the first term indicates the dipolar interactions of the magnetic moments. The second term shows the short-range magnetic exchange coupling. The third, fourth, and fifth terms indicate the contribution of local modes, AFD motions, and strain in magnetic exchange interaction, respectively. The sixth term shows the contribution of the tilting of oxygen octahedra through Dzyaloshinskii-Moriya interaction [42–44]. In addition to the energy contributions discussed above, if

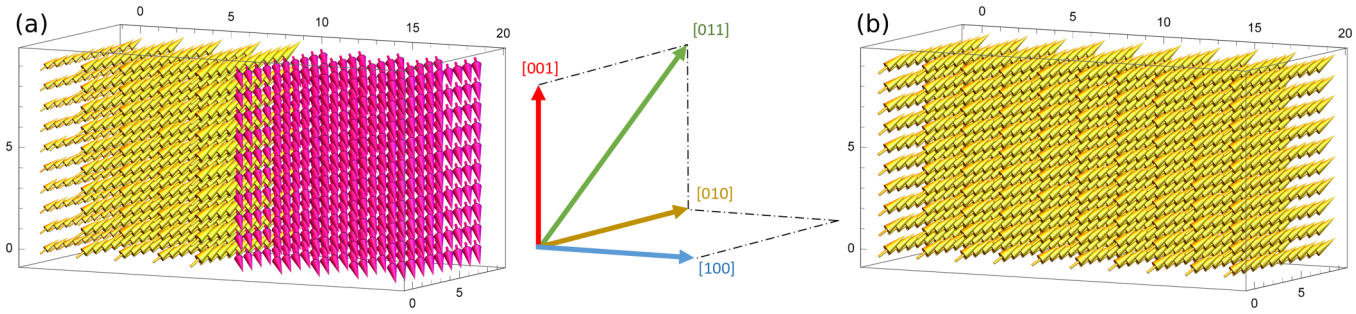

FIG. 1. Schematic representation of the electric dipole moments for a 20 × 10 × 10 supercell of $BiFeO_3$ (a) a multidomain structure in which electric dipole moments are initially along the [111] direction in the first (left) domain and along $[1\bar{1}\bar{1}]$ in the second (right) domain; (b) a monodomain structure in which all electric dipole moments are along the pseudocubic [111] direction.

external magnetic and/or electric fields are applied, their contribution to the energy as $-\sum_i \boldsymbol{m}_i \cdot \boldsymbol{H}$ for magnetic field and $-\sum_i \boldsymbol{P}_i \cdot \boldsymbol{E}$ for electric field should be added to the total energy terms. The electrical polarization, $\boldsymbol{P}$, can be computed from its proportionality to the local modes via $\boldsymbol{P} = \frac{Z^* \boldsymbol{u}}{V_0}$ in which Z^* is the Born effective charge obtained from first-principles calculations and its value for BFO is $Z^* = 5.68\,C$ [45], while V_0 is the volume of the unit cell.

To predict the dynamical properties of $BiFeO_3$ within the effective Hamiltonian framework used here, Newtonian equations of motion are applied for the ionic degrees of freedom (i.e., local modes, AFD, strains) discussed in Eq. (1) where the forces were computed by taking partial differential of the total energy terms similar to the techniques used in Refs. [46–48]. Moreover, as demonstrated in Ref. [13], the dynamics of the magnetic moments are considered through the Landau-Lifshitz-Gilbert equation [49] as indicated in the following:

$$\frac{d\boldsymbol{m}_i}{dt} = -\Gamma \boldsymbol{m}_i \times \left[\boldsymbol{B}^i_{\text{eff}}(t) + \boldsymbol{b}^i_{\text{fl}}(t)\right] - \Gamma \frac{\lambda}{|\boldsymbol{m}_i|(1+\lambda^2)} \boldsymbol{m}_i \times \left\{\boldsymbol{m}_i \times \left[\boldsymbol{B}^i_{\text{eff}}(t) + \boldsymbol{b}^i_{\text{fl}}(t)\right]\right\}. \quad (5)$$

Here, $\boldsymbol{B}^i_{\text{eff}}$ is the effective magnetic field which acts on the ith magnetic moment and is given by $\boldsymbol{B}^i_{\text{eff}} = -\partial E_{\text{tot}}/\partial \boldsymbol{m}_i$, while Γ and λ are gyromagnetic and damping coefficients, respectively. $\boldsymbol{b}^i_{\text{fl}}$ is is a fluctuation field which is also acting on the ith magnetic moment. More details on the dynamics of magnetic properties calculations are given in Ref. [13].

III. RESULTS AND DISCUSSION

A. Polarization, magnetization, and magnetoelectric coefficients

Here and as shown in Fig. 1(a), we investigate BFO with two domains separated by a 109° domain wall through a periodic 20 × 10 × 10 supercell (for comparison, Fig. 1(b) displays a monodomain). We have investigated 71° and 180° domain configurations as well, and the results of our analyses are consistent with 109° configurations. However, since 109° domain walls are the ones that are found most frequently in BFO bulk materials and the most seen ferroelastic domain walls in single crystal samples of BFO, the results for 109° configurations are shown and discussed here [50,51]. In Fig. 1(a), the left-hand side along the x axis (which lies along the pseudo-cubic [100] direction), is made of electric dipoles being initially along [111] while the right-hand side is formed by electric dipoles initially lying along $[1\bar{1}\bar{1}]$. This supercell is subjected to a magnetic field, $H = H_{\text{dc}} + h_{\text{ac}} \sin(\omega t)$, that is applied along the $[\bar{2}11]$ direction and which is a combination of a dc field with an ac field of ω frequency. We chose $H_{\text{dc}} = 245\,T$ and $h_{\text{ac}} = 61.2\,T$ to get good statistics on the quadratic ME coefficients since, for such fields, linear magnetoelectricity has a small effect with respect to the quadratic ME coefficients in BFO (see Refs. [36,38] and the Supplemental Material of Ref. [26]). However, and as shown in the Supplemental Material [52], the simulations were performed at lower magnetic fields to make sure that the observed results are still valid at magnetic fields that can be applied in practical applications.

Note that, in the entire supercell, the initial magnetization is along the $[\bar{2}11]$ direction, i.e., along which the magnetic field is applied, while the G-type antiferromagnetic vector is along the perpendicular $[01\bar{1}]$ direction. Furthermore, ω is fixed during each simulation, but is allowed to vary from 10 GHz to 1300 GHz between different computations. The upper limit of investigated frequencies is intentionally chosen such as to avoid resonating with the A_1 phonon frequencies (known to occur at much higher frequencies of the order of ∼4300 and ∼7000 GHz [25,53]), but also to focus on the possibility of having electromagnons associated with domain walls and thus occurring at lower frequencies (note that we do see these A_1 phonon frequencies in our simulations but do not report them here).

Note also that the homogeneous strain has been recently predicted to combine with optical phonons and magnons to create another quasiparticle, coined electroacoustic magnon, that can result in the emergence of resonance in the ME response [26]. Since we are especially interested here in revealing domain-wall-induced electromagnons (i.e., mixing of optical vibrations with magnons in a multidomain structure), we perform two kinds of MD simulations: one for which the homogeneous strain is clamped (implying that no electroacoustic magnon can exist) versus another for which such strain is fully relaxed. The inhomogeneous strain, on the other hand, is considered in the effective Hamiltonian and can vary during the course of all types of simulations conducted here.

Note also that, in multiferroics, the electrical polarization under the influence of applied electric and magnetic fields can be obtained by differentiating the expansion of the free

energy with respect to electric field [5]. In the absence of external applied electric fields and when neglecting the linear ME coefficient, the temporal evolution of the polarization as a function of our applied magnetic fields is given by

$$P(t) = P_{(t=0)} + \beta(0,\omega)H_{\rm dc}h_{\rm ac}\sin(\omega t) + \beta(\omega,\omega)\tfrac{1}{2}h_{\rm ac}^2\sin^2(\omega t). \quad (6)$$

where $\beta(0,\omega)$, on which we primarily focus, is the quadratic ME coefficient coupling the ac and dc fields, while $\beta(\omega,\omega)$ couples the ac field with itself and generates a second harmonic at 2ω.

The real and imaginary parts of $\beta(0,\omega)$ can thus be obtained by

$$\beta'(0,\omega) = \frac{\frac{2}{\tau}\int_0^\tau (P - P_{(t=0)})\sin(\omega t)dt}{H_{\rm dc}h_{\rm ac}} \quad (7)$$

and

$$\beta''(0,\omega) = \frac{\frac{2}{\tau}\int_0^\tau (P - P_{(t=0)})\cos(\omega t)dt}{H_{\rm dc}h_{\rm ac}}, \quad (8)$$

in which τ is the overall time of the simulation. More details about the derivation of Eqs. (7) and (8) are provided within the Supplemental Material.

B. Frequency analysis

Let us first consider the case of the aforementioned multidomain structure *when the homogeneous strain is clamped*. During and at the end of the simulation, the overall polarization is along the [100] direction, since the y and z components of the dipoles in the left and right domains cancel each other. Furthermore, the direction of the magnetic moments during and at the end of the simulation is found to be along the applied dc magnetic field, i.e., $[\bar{2}11]$, in both domains.

We then perform Fourier analysis of the temporal evolution of this electrical polarization and resulting magnetization along different directions (to, e.g., reveal the directions of vibration of phonons and magnons that are dynamically coupled to form electromagnons). Note that here we are dealing with two types of frequencies, one being the frequency of applied magnetic field which is denoted by ω, while the other is the frequency spectrum that we get as a result of Fourier analyses of the dynamical evolution of the polarization or magnetization under the applied field. For instance, the frequency spectra of the electrical [100]-component of the dipoles (direction of polarization, as well as normal to the ferroelectric domain wall) and the perpendicular, [011] component, when the frequency of the applied magnetic field, ω, is 10 GHz are demonstrated by red solid lines in Figs. 2(a) and 2(c), respectively, and up to about 1300 GHz. Apart from the frequency of applied field and its second harmonic at 10 and 20 GHz, two peaks are observed at ∼390 and ∼1150 GHz in the spectrum of the [100]-component [Fig. 2(a)]. Also a peak is observed at ∼700 GHz for the [011]-component [Fig. 2(c)].

In addition, the Fourier analyses of the magnetization were performed for the $[\bar{2}11]$-component which is also the direction of the magnetic moments and the applied magnetic field [Fig. 2(b)] as well as the $[01\bar{1}]$-component which is also a direction that is perpendicular to both polarization and magnetization [Fig. 2(d)]. Since the peaks at ∼390 GHz and ∼1150 GHz are present in the Fourier analyses of both the [100] component of polarization and $[\bar{2}11]$ component of magnetization, these peaks represent *electromagnons* for which the optical phonon has a component of its vibration along the direction that is perpendicular to the domain wall and the magnon has a component of its vibration along the magnetization. (It should be noted that,we found such electromagnons for the 71° domain configuration at ∼455 GHz and ∼1390 GHz. Also, for the 180° domain configuration, such electromagnons are found to be at 240 GHz and 1430 GHz). Similarly, the peaks at ∼700 GHz seen in Figs. 2(c) and 2(d) characterize an electromagnon made of an optical phonon that has a vibration direction with a component lying along the [011] direction and of a magnon for which the vibration has a finite component along $[01\bar{1}]$ (note that [011] and $[01\bar{1}]$ are both lying in the plane of the domain wall but are perpendicular to each other). Interestingly, and as verified by black solid lines in Figs. 2(a)–2(d), these three peaks disappear when the simulations are performed for the case of monodomain structure (whether the homogeneous strain is clamped or unclamped). In other words, one can conclude that the 390, 1150, and 700 GHz modes are *domain-wall-induced* electromagnons (to be denoted as DWI electromagnons in the following). Such observations are also consistent with previous findings that vibrations of the order of 360, 700, and ∼ 1200–1800 GHz caused by domain-wall motions were predicted for the case of BFO adopting domain structures [50,54] (note that other domain wall activities, but with lower frequencies, were also reported in Refs. [55,56] but the limitation of MD methods below the range of few GHz prevents us from determining them).

Figures 2(a)–2(d) also report the case of a multidomain but *for unclamped homogeneous strain*, which is represented by dashed blue lines. In this latter case, three additional peaks are observed at 70, 100, and 270 GHz with respect to the case of clamped multidomains, for the Fourier transform of the temporal evolution of the polarization and magnetization. These three peaks, therefore, indicate that strain can mix with optical lattice vibrations and magnons to produce new particles, which is in line with the recent prediction of the so-called electroacoustic magnons for unclamped monodomain in Ref. [25]. Note that these electroacoustic magnons at 70 and 270 GHz in our multidomain involve vibration of the polarization along the normal of the domain wall [see Fig. 2(a)] while that at 100 GHz is better seen in the oscillation of the electric dipoles perpendicularly to that normal [cf. Fig. 2(c)]. Moreover, the magnon associated with these electroacoustic magnons at 70, 100, and 270 GHz have vibrations along both $[\bar{2}11]$ (that are stronger) and $[01\bar{1}]$ (that are weaker), as demonstrated by Figs. 2(b) and 2(d).

C. Magnetoelectric response

Let us from now on focus on results obtained *for the case of unclamped homogeneous strain* in the multidomain structure, since we now know the origins of all the peaks appearing in Fig. 2. The real and imaginary parts of the quadratic ME

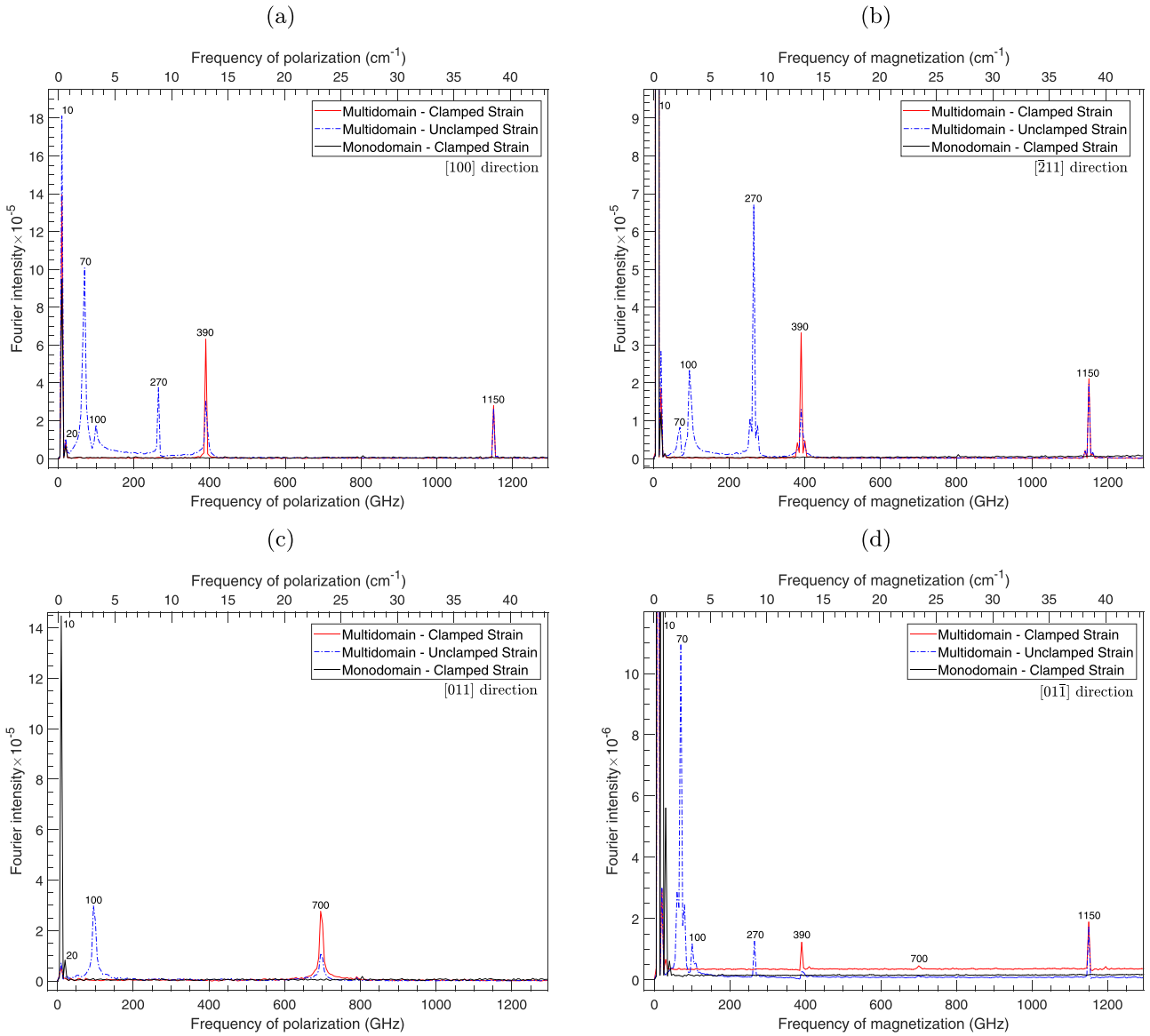

FIG. 2. The Fourier analyses of the polarization [(a) is for polarization along the [100] direction while (c) is for polarization along the [011] direction] and magnetization [(b) is for magnetization along the [$\bar{2}11$] direction while (d) is for magnetization along the [$01\bar{1}$] direction] for the case of monodomain when the strain is unclamped (black) and for the case of multidomain when the homogeneous strain is unclamped (blue) and clamped (red). Here, the frequency of the applied magnetic field is 10 GHz. Note the change of vertical scale between (b) and (d).

coefficient, $\beta(0,\omega)$, for polarization lying along the [100] and [011] directions, are then computed using Eqs. (7) and (8) at each frequency of applied magnetic field from 10 to 1300 GHz in that case. They are shown in Figs. 3(a) and 3(b), respectively. The calculated values are in agreement with experimental measurements of β of bulk BFO at small frequencies. For instance, the obtained value for the real part of $\beta(0,\omega)$ along the [100] direction by our MD simulations when the frequency of applied magnetic field is 20 GHz and the homogeneous strain is unclamped, is $2.457 \times 10^{-8}\, C/m^2T^2 = 0.388 \times 10^{-19}\, s/A$ which remarkably agrees with the observation of $\beta_{311} = 0.3 \times 10^{-19}\, s/A$ reported in Ref. [57] for the static case. Also, in measurements that were performed in high magnetic fields [58], the quadratic ME coefficient was found to be $\beta_{122} = \beta_{212} = \beta_{221} = -\beta_{111} = -5 \times 10^{-9}\, C/m^2T^2$, which is in reasonable agreement with the value of $-1.004 \times 10^{-9}\, C/m^2T^2$ that we have computed along the [011] direction at $\omega = 20$ GHz. The ME coefficients exhibit resonances when the frequency of applied magnetic field, ω, approaches the frequency of the electroacoustic-magnon-like particles mentioned above, that are 70, 100, and 270 GHz here, as previously found for the case of a monodomain, for which electroacoustic magnons have resonant frequencies at 90 and 267 GHz [25,26].

Moreover, another important novelty of the present paper is that resonances also happen when ω reaches the frequency of the three domain-wall-induced electromagnons. For instance, along the [011] direction, a nicely seen resonance takes place at $\omega = 700$ GHz, while, along the [100] direction, one resonance is rather sharp at 390 GHz while the other one around 1150 GHz is broader and even seems to be made of several peaks—which is reminiscent of the broad

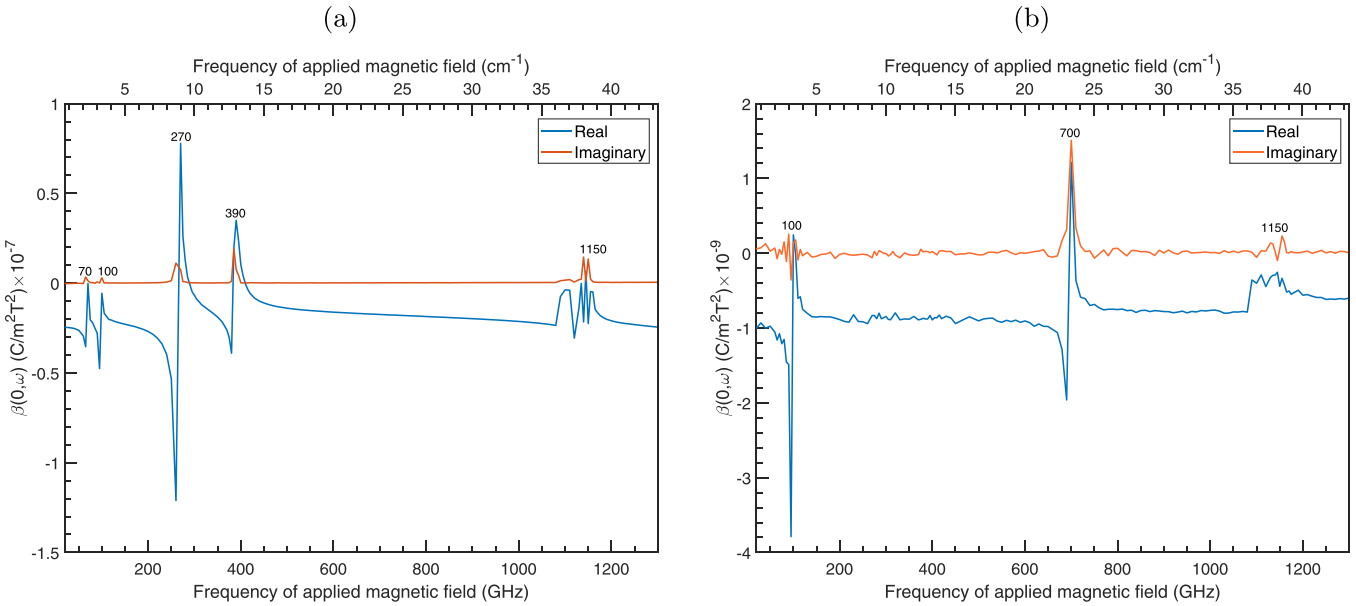

FIG. 3. Frequency dependence of the real and imaginary parts of the quadratic magnetoelectric coefficient $\beta(0,\omega)$ along (a) the [100] direction, and (b) the [011] direction when the homogeneous strain is unclamped. Note the change of vertical scale between (a) and (b).

response found in Ref. [54] around these frequencies for the domain wall motions. These results are also consistent with the dielectric and domain-wall-related modes *A* and *B* reported in Ref. [50] for which mode *A* around 12 $\text{cm}^{-1} \simeq$ 360 GHz is sharp while mode *B* around 50 $\text{cm}^{-1} \simeq 1500$ GHz is broader. Our DWI electromagnons therefore provide a path to engineer devices based on the functionality of the domain walls. Although domain walls have already been employed in spintronics and for designing devices [59–61], their presently discovered role in optimizing ME responses also make them fascinating for ME-based devices. As a matter of fact, our results show that one can tune the frequency of the applied magnetic field with the frequency of the domain wall vibrations (DWI electromagnons) to maximize the ME response.

D. Degree of localization of the domain-wall-induced electromagnons

To investigate the degree of localization that these DWI electromagnons possess, a layer-by-layer analysis is performed at different planes that are parallel to the domain wall. As the dimension of the supercell is $20 \times 10 \times 10$, each 10×10 cross section of the supercell along the [100] direction is defined as a layer for which the average of magnetization and polarization can be computed from the MD simulation results. Also, the quadratic ME coefficient of each layer can be obtained via Eqs. (7) and (8) but for which the overall polarization is replaced by the average polarization of each layer. The layers are indicated by their plane numbers, with the planes 10 and 20 corresponding to the domain wall layers

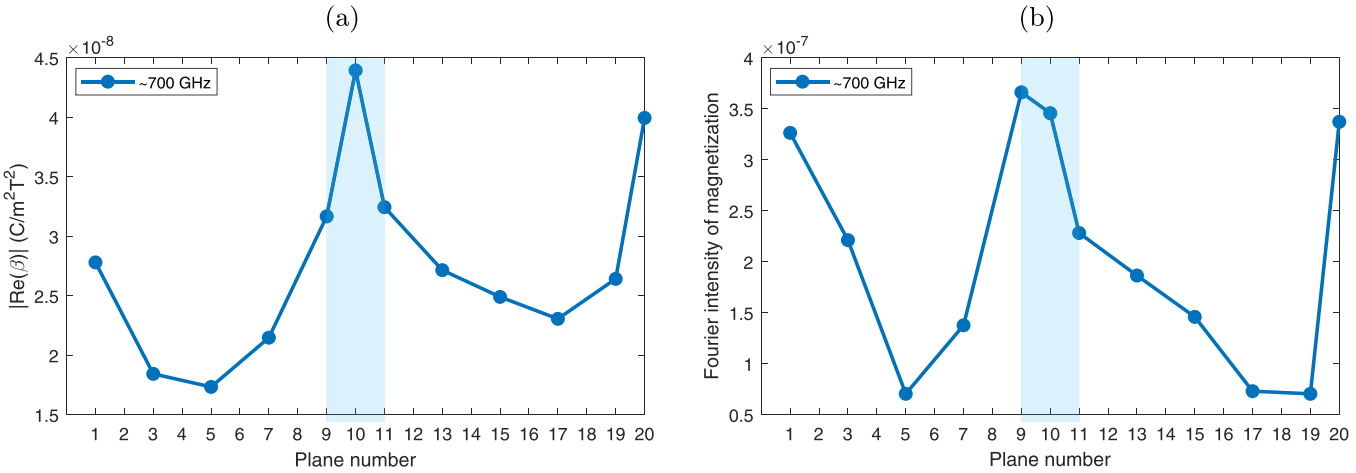

FIG. 4. Layer-by-layer analysis for the domain-wall-induced electromagnons at 700 GHz. Layer-by-layer comparison of the intensity of (a) the resonance peaks of the real part of ME coefficient, β, along the [011] direction when the frequency of applied magnetic field is 700 GHz and (b) Fourier peaks around 700 GHz for magnetization vibrations along the $[01\bar{1}]$ direction. For (b), the frequency of applied magnetic field is 10 GHz.

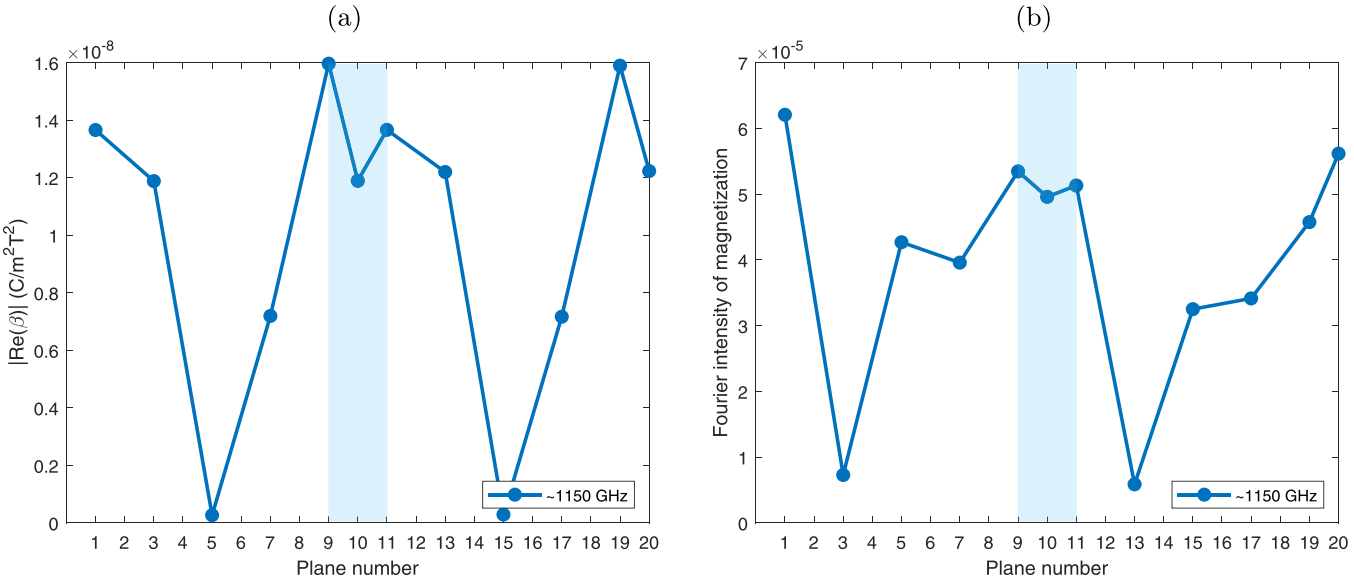

FIG. 5. Layer-by-layer analysis for the domain-wall-induced electromagnons at 1150 GHz. (a) shows the magnetoelectric coefficient, β, along the [100] direction when the frequency of applied magnetic field is 1150 GHz;. (b) shows the Fourier spectrum of magnetization along the $[\bar{2}11]$ direction for 1150 GHz. For (b), the frequency of applied magnetic field is 10 GHz.

whereas planes 5 and 15 correspond to the center of each domain. Since the ME coefficients $\beta(0,\omega)$ are calculated at each frequency of applied magnetic field for frequencies up to 1300 GHz, in each plane that is parallel to the domain wall, the absolute value of the real part of the ME coefficient, $|\mathrm{Re}(\beta(0,\omega))|$ (which is related to real-space location of optical phonons) is used to investigate the preferential location of the optical phonons. On the other hand, for each frequency of applied magnetic field, the Fourier analysis of magnetic moments provides a spectrum of the frequencies that are present in the vibration of the magnetic moments. Therefore, the Fourier intensity of the magnetization which is related to real-space location of magnons is used to investigate the preferential location of magnons. Here we used the Fourier analyses when the frequency of applied magnetic field is 10 GHz.

Figures 4(a) and 4(b) provide an example of the results on such analysis for the optical phonon [Fig. 4(a)] and magnon [Fig. 4(b)] associated with the frequency of 700 GHz. One can see that the maximum value of the resonance peak inside the domain (plane 5), which is $1.732 \times 10^{-8}\, C/m^2T^2$, jumps to $4.393 \times 10^{-8}\, C/m^2T^2$ at the domain wall (plane

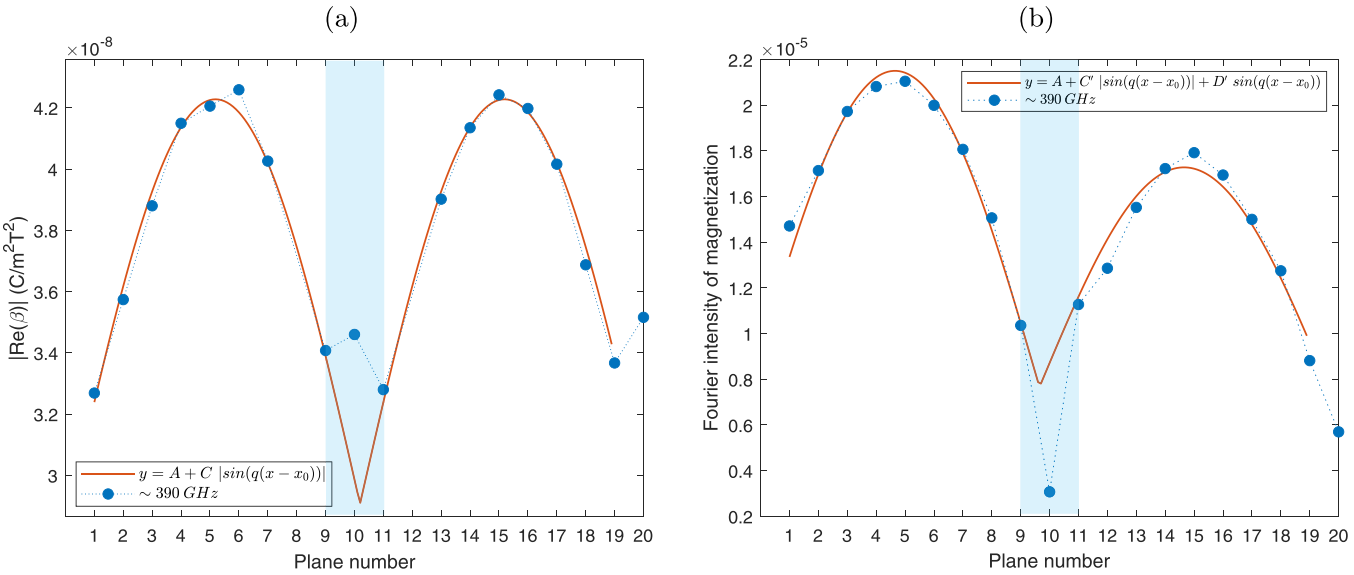

FIG. 6. Layer-by-layer analysis for the domain-wall-induced electromagnons at 390 GHz Layer-by-layer comparison of the intensity of the (a) resonance peaks of the real part of ME coefficient, β, along the [100] direction when the frequency of applied magnetic field is 390 GHz; (b) Fourier peaks around 390 GHz for magnetization vibrations along the $[\bar{2}11]$ direction. For (b), the frequency of applied magnetic field is 10 GHz.

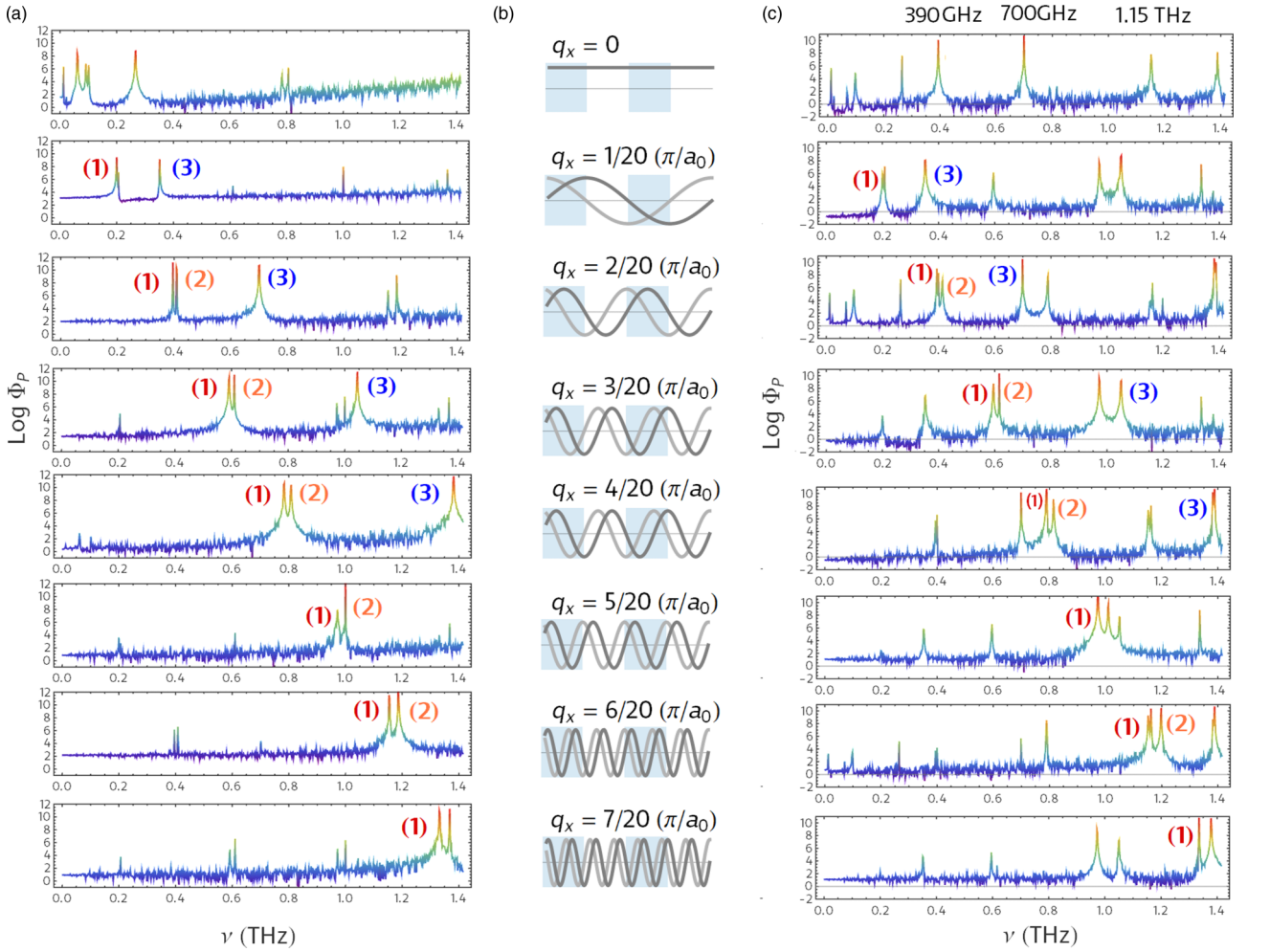

FIG. 7. Low-frequency spectrum of polar excitations for monodomain and multidomain states. Each subpanel in (a) and (c) shows the dependence of the logarithm of the spectral energy density Φ_P on frequency at a single wave vectors $\mathbf{q} = (q_x, 0, 0)$. (1)–(3) indicate the relevant electromagnon branches. The value of q_x for each row of subpanels is indicated in (b). (b) also contains a schematic representation of a $40 \times 10 \times 10$ supercell with four alternating domains (blue and white regions) along with examples of the $\mathbf{q}$-wave modulations.

10), showing that the ME coefficient is increased by 154%. Such comparison clarifies that not only the ME coefficient exhibits a resonance when the frequency of applied magnetic field is 700 GHz, but also the resonance is intensified at the domain walls. Furthermore, Fig. 4(b) compares the intensity of Fourier analyses peaks around 700 GHz for magnetization along the $[01\bar{1}]$ direction in each layer. The Fourier intensity of vibrations of magnetization at $\omega = 700$ GHz is stronger at the domain wall. Consequently, one can conclude that the DWI electromagnon at $\omega = 700$ GHz can be seen as waves that adopt a maximum at the domain wall, that is both the optical phonon and magnon forming such electromagnons preferentially localize at this ferroelectric domain wall. Such domain-wall-induced electromagnon wave behavior and preferential localization are also found for the frequency of 1150 GHz (but for optical phonon vibrating along [100] and magnons oscillating along $[\bar{2}11]$). As a matter of fact, and as demonstrated in Figs. 5(a) and 5(b), both the optical phonon and magnon of the domain-wall-induced electromagnon at 1150 GHz adopt wavelike behavior with maxima occurring in the vicinity of the domain walls (near plane 10). On the other hand, the DWI electromagnon having a resonant frequency of 390 GHz while still possessing wavelike behavior, prefers to possess maxima occurring, both for its optical phonon and magnon, *near the middle of the domains* (near planes 5 and 15) rather than at the domain wall, as demonstrated in Figs. 6(a) and 6(b). Note that the Supplemental Material also reports information about localization/delocalization of the electroacoustic magnons and some results on inhomogeneous strain analysis.

E. The origin of the domain-wall-induced electromagnons

To have a clear understanding of the origin of the 390 GHz, 700 GHz, and 1150 GHz electromagnons induced by the domain structure, we have analyzed the spectral energy density (SED) associated with local dipoles (Φ_P) and inhomogeneous stain (Φ_η) when the homogeneous strain was unclamped and for a $40 \times 10 \times 10$ supercell. To conserve the periodicity of the domain structure, the supercell is split into four alternating domains of equal width. Note that a larger supercell (i.e., $40 \times 10 \times 10$ as compared to $20 \times 10 \times 10$) is used to increase the wave vector q resolution. Note also that Φ_X, with $X{=}P$ or η, describes the wave vector $\mathbf{q}$ and frequency

ν resolved power of the kinetic energy spectrum for the vector degrees of freedom X. It is computed [62] as

$$\Phi_X(\mathbf{q}) = \frac{1}{N\tau} \sum_{\alpha=x,y,z} \left|\dot{X}^{\alpha}_{\mathbf{q},\nu}\right|^2, \tag{9}$$

where $\dot{X}^{\alpha}_{\mathbf{q},\nu}$ denotes the fast Fourier transform coefficient of the α component of the velocity $\dot{X}^{\alpha}$. N and τ denote the total number of unit cells and the MD trajectory time, respectively. The poles of Φ_P provide the spectrum of excitations independently of the mode's polarization vector. Specifically, Φ_P and Φ_η can be used to obtain dispersions of optical and acoustic phonons, respectively.

Practically, we use a single 0.5 ns MD trajectory computed for this $N = 40 \times 10 \times 10$ supercell. The integration time step is taken to be equal to 0.5 fs and the first 10000 steps of the trajectory are not taken into consideration. The velocities are sampled each 10 MD steps for subsequent fast Fourier transforms to the wave vector and frequency domain.

Figures 7(a) and 7(c) show the computed low-frequency spectra of polar excitations along the [100] pseudocubic direction (i.e., different panels on the left (right) side correspond to different q points along that direction) for mono- and multidomain states, respectively. The spectrum for the monodomain configuration [Fig. 7(a)] clearly shows the dispersion of three electromagnon branches labeled (1)–(3). From the analysis of Φ_η, we also find that these branches follow the dispersion curves of acoustic phonons (not shown here). Branches (1) and (2) match the two transverse acoustic (TA) modes, while the third branch is mixed with the longitudinal acoustic mode.

Interestingly, the three described monodomain branches can also be clearly seen in the spectrum of the multidomain state [see Fig. 7(c)]. However, the multidomain spectrum additionally features multiple satellite peaks not present in the monodomain case [Fig. 7(a)]. These features most likely stem from the elastic scattering of the three monodomain electromagnons by a periodic and static array of domain walls. In such a hypothetical scenario, a single scattering event would conserve the mode frequency and lead to a shift of its momentum q_x by $\pm\Delta q_x$. The possible shifts

$$\Delta q_x = \frac{2}{20}\frac{\pi}{a_0}, \frac{6}{20}\frac{\pi}{a_0}, \frac{10}{20}\frac{\pi}{a_0} \tag{10}$$

correspond to the dominant Fourier components of the local mode distribution or, in other words, are determined by the periodicity of the domain structure. Here a_0 indicates the five-atom lattice constant.

The simplest single scattering mechanism described above allows us to explain the appearance of the predicted domain-wall-induced electromagnons at $q_x = 0$, namely, the emergent zone-center excitations at 390 GHz and 700 GHz can be matched with monodomain modes (1) and (3) at $q_x = \frac{2}{20}\frac{\pi}{a_0}$ that are scattered by $\Delta q_x = -\frac{2}{20}\frac{\pi}{a_0}$ [see Figs. 8(a) and 8(b)], while the homogeneous 1150 GHz mode stems from scattering of mode (1) at $q_x = \frac{6}{20}\frac{\pi}{a_0}$ by $\Delta q_x = -\frac{6}{20}\frac{\pi}{a_0}$ [see Figs. 8(a) and 8(c).

Such hypothesis about the origin of the domain-wall-induced electromagnons is further supported by visualizing the local mode vibrations at $\nu_0 = 390$ GHz, 700 GHz, and 1150 GHz. To perform this analysis, we first note the deviation

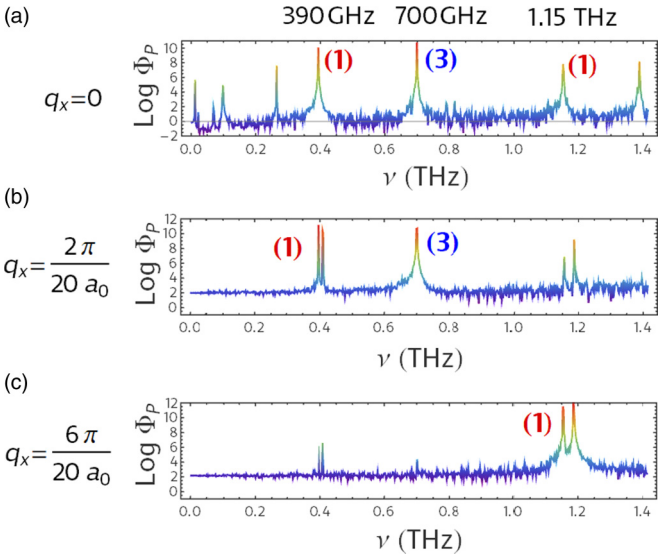

FIG. 8. Origin of the zone-center electromagnons. (a) shows the logarithm of the optical phonon SED at $q_x = 0$ for the multidomain state. (b), (c) show the logarithm of the optical phonon SED for the monodomain state at $q_x = \frac{2}{20}\frac{\pi}{a_0}$ and $q_x = \frac{6}{20}\frac{\pi}{a_0}$, respectively. Labels (1) and (3) indicate the matching frequencies of the mode before [(b), (c)] and after a single scattering event (a).

of the average local mode value $\delta\mathbf{u}(x,t) = \mathbf{u}(x,t) - \langle\mathbf{u}(x)\rangle$ within each x layer of the supercell and at each MD step t from its time average $\langle\mathbf{u}(x)\rangle$. Then we perform the time-frequency Fourier transformation $\delta\mathbf{u}(x,t) \to \delta\mathbf{u}(x,\nu)$ that allows us to look at how the layer-averaged local modes change along the [100] direction and only at the frequencies of interest (i.e., at these ν_0). We perform the described procedure using the generated MD trajectories for the multidomain case which technically corresponds to isolating the excitations pattern at a specific frequency in Fig. 7(c). Figure 9 shows how the resulting complex amplitudes $\delta u_\alpha(x,\nu_0)$ and phases $\theta_\alpha = \arg(\delta\mathbf{u}_\alpha(x,\nu_0))$ change with x for each Cartesian component α of the local modes.

As expected from the scattering picture, the amplitudes of local modes displacements at $\nu_0 = 390$ GHz [Fig. 9(a)] and $\nu_0 = 700$ GHz [Fig. 9(b)] have a pronounced $q_x = \frac{2}{20}\frac{\pi}{a_0}$ character with half of the wave period falling within each of the domains [Fig. 7(b)]. At the same time, and as also consistent with Fig. 8(c), the amplitudes $\delta u_\alpha(x,\nu_0)$ at $\nu_0 = 1150$ GHz [see Fig. 9(c)] have a different, three half-period character rather described by $q_x = \frac{6}{20}\frac{\pi}{a_0}$ [Fig. 7(b)]. This latter periodicity is more clearly visible in the dependence of the phase on x at $\nu_0 = 1150$ GHz [see Fig. 9(f)].

It is also interesting to note the markedly distinct behavior of the phase plots at $\nu_0 = 390$ GHz and $\nu_0 = 1150$ GHz from the complex phase distribution at $\nu_0 = 700$ GHz. Indeed, the two former feature a constant (flat) phase $\theta_\alpha(x)$ dependencies on x within each domain [Figs. 9(d) and 9(f)]. Such distribution along with spatially modulated amplitudes [Figs. 9(a) and 9(c)] are unique signatures of standing waves. Notably, the standing-wave character (confinement) of these modes also goes in line with the TA nature of the original monodomain branch (1) giving rise to these modes. Indeed, similar

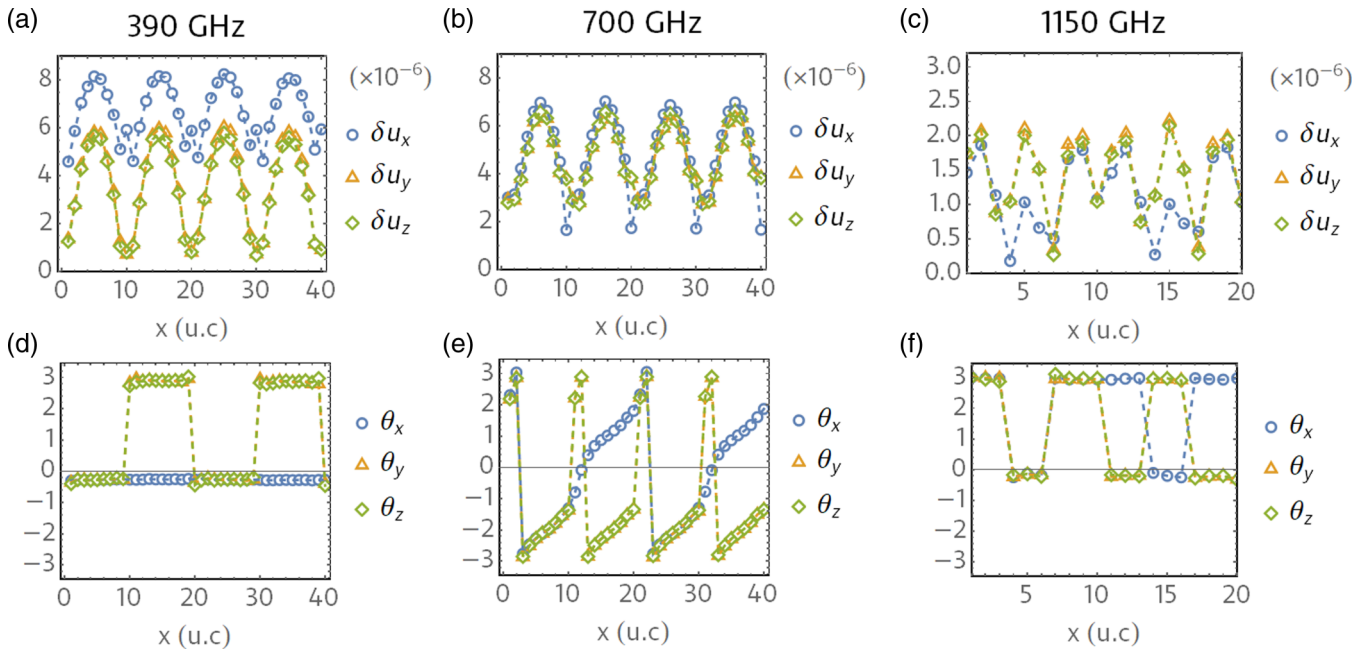

FIG. 9. Analysis of local mode vibrations at emergent electromagnon frequencies. (a)–(c) [(d)–(f)] show the changes of the complex amplitude (phase) of the local mode vibrations along the [100] direction at 390 GHz, 700 GHz, and 1150 GHz, respectively.

situations were previously reported in Refs. [63,64] describing the confinement of TA acoustic phonons in semiconductor superlattices. In contrast, the $\nu_0 = 700$ GHz vibration pattern rather corresponds to a propagating wave as the latter typically yields a linear phase dependence on the coordinate [see Fig. 9(e)]. This observation also goes in line with our prediction of the common origin of the $\nu_0 = 390$ GHz and $\nu_0 = 1150$ GHz electromagnons distinct from that of the $\nu_0 = 700$ GHz domain-wall-induced mode. Finally, from Fig. 9 it can be further noted that for all of the considered frequencies, the vibration patterns are neither the classical standing nor classical propagating waves. Indeed, the amplitude plots in Fig. 9 clearly indicate that all modes are mixed with Gamma point vibrations while the amplitude deviations at the domain walls indicate the presence of domain-wall localized modes. Moreover, the phase velocity of the propagating electromagnon at $\nu_0 = 700$ GHz clearly increases upon approaching the domain walls [Fig. 9(e)] while, at the same time, its amplitude experiences a drop. Such change of the phase velocity can be equivalently described as a mixing of the propagating mode with a domain-wall localized mode and a standing wave at $q_x = \frac{2}{20}\frac{\pi}{a_0}$. All of the described deviations are due to the aforementioned scattering which couples phonons with wave vectors differing by the multiples of $\frac{2}{20}\frac{\pi}{a_0}$ due to which all of the three modes have a mixed character. To complete the picture, we summarize the information presented in Fig. 9 by plotting the instantaneous snapshots of the calculated profiles of dipole vibrations at $\nu_0 = 390$ GHz, 700 GHz and 1150 GHz in Fig. 10.

Based on the gathered insights, we now fit (as an example) the values of the Fourier intensity peaks of ME coefficient, $\beta(0, \omega)$, along the [100] direction and at 390 GHz by a function of the form

$$y = A + C|sin(q(x - x_0))|, \tag{11}$$

where $q = \frac{2}{20}\frac{\pi}{a_0}$ is the scattering vector for that frequency, A is the amplitude of the zone-center mode and C can be seen as an x-component amplitude of the confined electromagnon at q. One can clearly see that such function fits well the data of Fig. 6(a), which confirms our proposed concept of scattering. Similarly, the values of the Fourier intensity peaks of magnetization along the $[\bar{2}11]$ direction at 390 GHz were fitted by a function of the form

$$y = A + C'|\sin(q(x - x_0))| + D'\sin(q(x - x_0)), \tag{12}$$

where q is still equal to $\frac{2}{20}\frac{\pi}{a_0}$, C' is related to the x-component contribution of the electromagnon as in Eq. (11), while D' originates from its y and z components. Once again, this function fits well the data of Fig. 6(b), which is another confirmation that scattering is the main source of the domain-wall-induced electromagnons. It should be noted that the difference between the data and the fit at domain walls comes from the modes localized on the domain walls.

IV. SUMMARY

In summary, we report here the existence and explain the origin of domain-wall-induced electromagnons, and discover that they enhance the ME response of the material to the application of external magnetic fields. Obtaining such results for bisumth ferrite not only implies that ME enhancement can be achieved at room temperature, but also infers that such enhancement can be generalized to other multiferroics possessing multidomains. Interestingly, the optical phonon and magnons forming such domain-wall-induced electromagnons behave as waves for which the maxima jointly occur in some specific parts of the multidomain, namely, near the domain walls for the 700 and 1150 GHz frequencies *versus* near the middle of each domain for the 390 GHz frequency. The presently discovered domain-wall-induced electromagnons

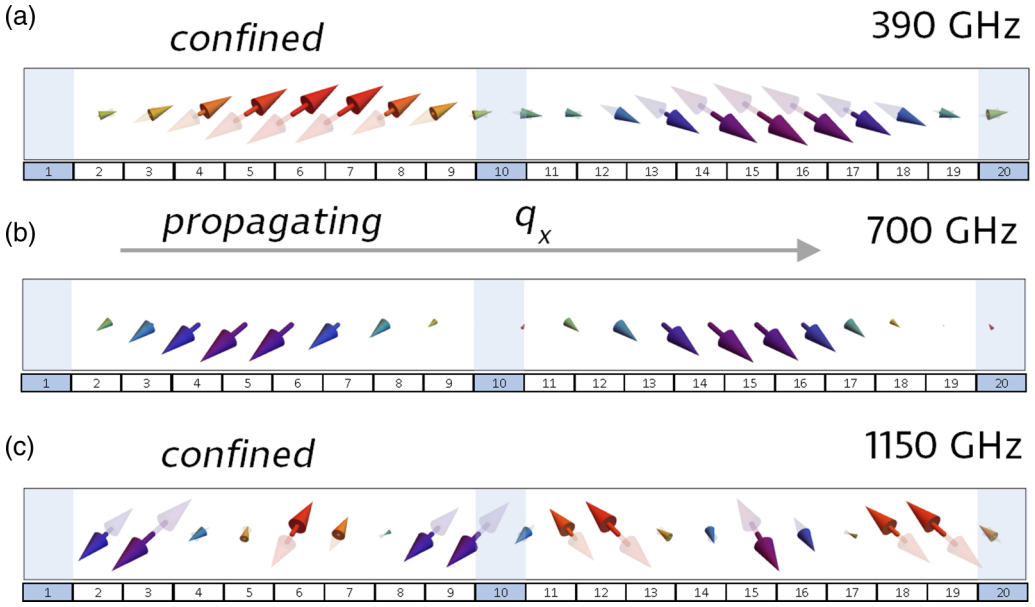

FIG. 10. Instantenous distribution of the local mode deviation vectors for the three considered domain-wall-induced electromagnons. The arrows indicate the local mode deviations with red (purple) color corresponding to vector with positive (negative) z components. Electromagnons at 390 GHz and 1150 GHz originate from the same monodomain electromagnon branch and have predominantly confined (standing-wave) character. The 700 GHz domain-wall-induced mode features a pronounced propagating wave nature.

may thus be of some advantages for, e.g., the design of (i) novel ultrafast energy-efficient data storage devices via local probes and (ii) and of electrically driven configurable magnonic circuits taking advantage of the spatial preferential localization of both the phonons and magnons making the domain-wall-induced electromagnons.

ACKNOWLEDGMENTS

The authors are thankful to Vannevar Bush Faculty Fellowship (VBFF) Grant No. N00014-20-1-2834 from the Department of Defense and the ARO Grant No. W911NF-21-1-0113. S.P. also thanks ONR Grant No. N00014-21-1-2086. B.X. further acknowledges the financial support from National Natural Science Foundation of China under Grant No. 12074277, the startup fund from Soochow University, and the support from Priority Academic Program Development (PAPD) of Jiangsu Higher Education Institutions. S.P. and Y.N. thank DARPA Grant No. HR0011727183-D18AP00010 (under the TEE Program). C.P. thanks the ANR Grant No. ANR-21-CE24-0032 SUPERSPIN, and a public grant overseen by the ANR as part of the Investissements d'Avenir program (Reference: ANR-10-LABX-0035, Labex-NanoSaclay). The authors are also thankful for the support of MRI Grant No. 0722625 from NSF, ONR Grant No. N00014-15-1-2881 (DURIP), as well as a Challenge grant from the Department of Defense, and also acknowledge the High Performance Computing Center at the University of Arkansas.

[1] Y. Tokura and S. Seki, Adv. Mater. **22**, 1554 (2010).
[2] S.-W. Cheong and M. Mostovoy, Nat. Mater. **6**, 13 (2007).
[3] T. Kimura, T. Goto, H. Shintani, K. Ishizaka, T.-h. Arima, and Y. Tokura, Nature (London) **426**, 55 (2003).
[4] Y. Takahashi, R. Shimano, Y. Kaneko, H. Murakawa, and Y. Tokura, Nat. Phys. **8**, 121 (2012).
[5] M. Fiebig, J. Phys. D **38**, R123 (2005).
[6] A. Kumar, J. Scott, and R. S. Katiyar, Appl. Phys. Lett. **99**, 062504 (2011).
[7] J. Wang, J. Neaton, H. Zheng, V. Nagarajan, S. Ogale, B. Liu, D. Viehland, V. Vaithyanathan, D. Schlom, U. Waghmare *et al.*, Science **299**, 1719 (2003).
[8] W. Eerenstein, N. Mathur, and J. F. Scott, Nature (London) **442**, 759 (2006).
[9] D. Lebeugle, D. Colson, A. Forget, M. Viret, A. M. Bataille, and A. Gukasov, Phys. Rev. Lett. **100**, 227602 (2008).
[10] G. Catalan and J. F. Scott, Adv. Mater. **21**, 2463 (2009).
[11] D. Khomskii, Physics **2**, 20 (2009).
[12] E. Albisetti, S. Tacchi, R. Silvani, G. Scaramuzzi, S. Finizio, S. Wintz, C. Rinaldi, M. Cantoni, J. Raabe, G. Carlotti *et al.*, Adv. Mater., **32** 1906439 (2020).
[13] D. Wang, J. Weerasinghe, and L. Bellaiche, Phys. Rev. Lett. **109**, 067203 (2012).
[14] Y. Zhang, Y. Zhang, Q. Guo, D. Zhang, S. Zheng, M. Feng, X. Zhong, C. Tan, Z. Lu, J. Wang *et al.*, Phys. Chem. Chem. Phys. **21**, 21381 (2019).
[15] R. Valdes Aguilar, A. B. Sushkov, C. L. Zhang, Y. J. Choi, S.-W. Cheong, and H. D. Drew, Phys. Rev. B **76**, 060404 (2007).
[16] R. de Sousa and J. E. Moore, Phys. Rev. B **77**, 012406 (2008).
[17] Z. Chen, M. Schmidt, Z. Wang, F. Mayr, J. Deisenhofer, A. A. Mukhin, A. M. Balbashov, and A. Loidl, Phys. Rev. B **93**, 134406 (2016).

[18] A. Pimenov, A. Mukhin, V. Y. Ivanov, V. Travkin, A. Balbashov, and A. Loidl, Nat. Phys. **2**, 97 (2006).

[19] A. B. Sushkov, R. V. Aguilar, S. Park, S.-W. Cheong, and H. D. Drew, Phys. Rev. Lett. **98**, 027202 (2007).

[20] T. Kubacka, J. A. Johnson, M. C. Hoffmann, C. Vicario, S. De Jong, P. Beaud, S. Grübel, S.-W. Huang, L. Huber, L. Patthey *et al.*, Science **343**, 1333 (2014).

[21] M. Cazayous, Y. Gallais, A. Sacuto, R. de Sousa, D. Lebeugle, and D. Colson, Phys. Rev. Lett. **101**, 037601 (2008).

[22] M. K. Singh, R. S. Katiyar, and J. Scott, J. Phys.: Condens. Matter **20**, 252203 (2008).

[23] A. Kumar, N. Murari, and R. Katiyar, Appl. Phys. Lett. **92**, 152907 (2008).

[24] C.-M. Chang, B. K. Mani, S. Lisenkov, and I. Ponomareva, Ferroelectrics **494**, 68 (2016).

[25] S. O. Sayedaghaee, B. Xu, S. Prosandeev, C. Paillard, and L. Bellaiche, Phys. Rev. Lett. **122**, 097601 (2019).

[26] S. O. Sayedaghaee, C. Paillard, S. Prosandeev, B. Xu, and L. Bellaiche, npj Comput. Mater. **6**, 60 (2020).

[27] T. Hoffmann, P. Thielen, P. Becker, L. Bohatý, and M. Fiebig, Phys. Rev. B **84**, 184404 (2011).

[28] S. L. Johnson, R. A. deSouza, U. Staub, P. Beaud, E. Mohr-Vorobeva, G. Ingold, A. Caviezel, V. Scagnoli, W. F. Schlotter, J. J. Turner, O. Krupin, W. S. Lee, Y. D. Chuang, L. Patthey, R. G. Moore, D. Lu, M. Yi, P. S. Kirchmann, M. Trigo, P. Denes, D. Doering, Z. Hussain, Z. X. Shen, D. Prabhakaran, and A. T. Boothroyd, Phys. Rev. Lett. **108**, 037203 (2012).

[29] I. Handayani, R. Tobey, J. Janusonis, D. Mazurenko, N. Mufti, A. Nugroho, M. Tjia, T. Palstra, and P. Van Loosdrecht, J. Phys.: Condens. Matter **25**, 116007 (2013).

[30] D. S. Rana, I. Kawayama, K. Mavani, K. Takahashi, H. Murakami, and M. Tonouchi, Adv. Mater. **21**, 2881 (2009).

[31] M. Mochizuki and N. Nagaosa, Phys. Rev. Lett. **105**, 147202 (2010).

[32] A. V. Chumak, V. I. Vasyuchka, A. A. Serga, and B. Hillebrands, Nat. Phys. **11**, 453 (2015).

[33] K. Wagner, A. Kákay, K. Schultheiss, A. Henschke, T. Sebastian, and H. Schultheiss, Nat. Nanotechnol. **11**, 432 (2016).

[34] S. Prosandeev, D. Wang, W. Ren, J. Íñiguez, and L. Bellaiche, Adv. Funct. Mater. **23**, 234 (2013).

[35] D. Edwards, N. Browne, K. M. Holsgrove, A. B. Naden, S. O. Sayedghaee, B. Xu, S. Prosandeev, D. Wang, D. Mazumdar, M. Duchamp *et al.*, Nanoscale **10**, 17629 (2018).

[36] S. Lisenkov, I. A. Kornev, and L. Bellaiche, Phys. Rev. B **79**, 012101 (2009).

[37] A. Apostolov, I. Apostolova, S. Trimper, and J. Wesselinowa, Phys. Status Solidi B **254**, 1600433 (2017).

[38] I. A. Kornev, S. Lisenkov, R. Haumont, B. Dkhil, and L. Bellaiche, Phys. Rev. Lett. **99**, 227602 (2007).

[39] W. Zhong, D. Vanderbilt, and K. M. Rabe, Phys. Rev. Lett. **73**, 1861 (1994).

[40] W. Zhong, D. Vanderbilt, and K. M. Rabe, Phys. Rev. B **52**, 6301 (1995).

[41] I. A. Kornev, L. Bellaiche, P.-E. Janolin, B. Dkhil, and E. Suard, Phys. Rev. Lett. **97**, 157601 (2006).

[42] B. Xu, B. Dupé, C. Xu, H. Xiang, and L. Bellaiche, Phys. Rev. B **98**, 184420 (2018).

[43] H. Katsura, N. Nagaosa, and A. V. Balatsky, Phys. Rev. Lett. **95**, 057205 (2005).

[44] A. Raeliarijaona, S. Singh, H. Fu, and L. Bellaiche, Phys. Rev. Lett. **110**, 137205 (2013).

[45] D. Rahmedov, Ph.D. thesis, Properties of Multiferroic Bismuth Iron Oxide from First Principles, University of Arkansas, United States, 2014.

[46] I. Ponomareva, L. Bellaiche, T. Ostapchuk, J. Hlinka, and J. Petzelt, Phys. Rev. B **77**, 012102 (2008).

[47] D. Wang, J. Weerasinghe, L. Bellaiche, and J. Hlinka, Phys. Rev. B **83**, 020301(R) (2011).

[48] D. Wang, E. Buixaderas, J. Íñiguez, J. Weerasinghe, H. Wang, and L. Bellaiche, Phys. Rev. Lett. **107**, 175502 (2011).

[49] J. L. García-Palacios and F. J. Lázaro, Phys. Rev. B **58**, 14937 (1998).

[50] J. Hlinka, M. Paściak, S. Körbel, and P. Marton, Phys. Rev. Lett. **119**, 057604 (2017).

[51] F. Borodavka, J. Pokorny, and J. Hlinka, Phase Transitions **89**, 746 (2016).

[52] See Supplemental Material at http://link.aps.org/supplemental/10.1103/PhysRevMaterials.6.034403 for more details on the derivations of the quadratic magnetoelectric coefficients, preferential location of the electroacoustic magnons, more details on inhomogeneous strain, the effect of geometry on the frequencies associated with electroacoustic magnons and domain-wall induced electromagnons, and results of simulations at lower magnetic fields as well as simulations at 300 K.

[53] H. Fukumura, S. Matsui, H. Harima, T. Takahashi, T. Itoh, K. Kisoda, M. Tamada, Y. Noguchi, and M. Miyayama, J. Phys.: Condens. Matter **19**, 365224 (2007).

[54] S. Prosandeev, Y. Yang, C. Paillard, and L. Bellaiche, npj Comput. Mater. **4**, 8 (2018).

[55] P. Chen, L. Ponet, K. Lai, R. Cingolani, and S. Artyukhin, npj Comput. Mater. **6**, 48 (2020).

[56] Y.-L. Huang, L. Zheng, P. Chen, X. Cheng, S.-L. Hsu, T. Yang, X. Wu, L. Ponet, R. Ramesh, L.-Q. Chen *et al.*, Adv. Mater. **32**, 1905132 (2020).

[57] C. Tabares-Muñoz, J.-P. Rivera, A. Bezinges, A. Monnier, and H. Schmid, Jpn. J. Appl. Phys. **24**, 1051 (1985).

[58] Y. F. Popov, A. Kadomtseva, S. Krotov, D. Belov, G. Vorob'ev, P. Makhov, and A. Zvezdin, Low Temp. Phys. **27**, 478 (2001).

[59] K.-J. Kim, S. K. Kim, Y. Hirata, S.-H. Oh, T. Tono, D.-H. Kim, T. Okuno, W. S. Ham, S. Kim, G. Go *et al.*, Nat. Mater. **16**, 1187 (2017).

[60] O. Gomonay, T. Jungwirth, and J. Sinova, Phys. Rev. Lett. **117**, 017202 (2016).

[61] H. Awano, J. Magn. Magn. Mater. **383**, 50 (2015).

[62] J. A. Thomas, J. E. Turney, R. M. Iutzi, C. H. Amon, and A. J. H. McGaughey, Phys. Rev. B **81**, 081411(R) (2010).

[63] C. Colvard, T. A. Gant, M. V. Klein, R. Merlin, R. Fischer, H. Morkoc, and A. C. Gossard, Phys. Rev. B **31**, 2080 (1985).

[64] M. V. Klein, IEEE J. Quantum Electron. **22**, 1760 (1986).